Implementation of contact line motion based on the phase-field lattice Boltzmann method

Long Ju [1], Zhaoli Guo [2], Bicheng Yan [3,*] and Shuyu Sun[1,†]

[1]*Computational Transport Phenomena Laboratory (CTPL), King Abdullah University of Science and Technology (KAUST), Thuwal, 23955-6900, Kingdom of Saudi Arabia*

[2]*Institute of Interdisciplinary Research for Mathematics and Applied Science, Huazhong University of Science and Technology, Wuhan 430074, China*

[3]*Energy Resource and Petroleum Engineering Program, Physical Science and Engineering Division, King Abdullah University of Science and Technology (KAUST), Thuwal, 23955-6900, Kingdom of Saudi Arabia*

This paper proposes a strategy to implement the free-energy-based wetting boundary condition within the phase-field lattice Boltzmann method. The greatest advantage of the proposed method is that the implementation of contact line motion can be significantly simplified while still maintaining good accuracy. For this purpose, the liquid-solid free energy is treated as a part of the chemical potential instead of the boundary condition, thus avoiding complicated interpolations with irregular geometries. Several numerical testing cases, including droplet spreading processes on the idea flat, inclined, and curved boundaries, are conducted, and the results demonstrate that the proposed method has good ability and satisfactory accuracy to simulate contact line motions.

I. INTRODUCTION

Multiphase flows are frequently encountered in industrial operations and engineering applications, such as enhanced oil recovery [1,2], geological carbon sequestration [3–5], geothermal [6], as well as underground hydrogen storage [7,8]. In these processes, the contact-line dynamics have long been of interest to the fluid research community, and intensive theoretical [9–11], experimental [12–14], and numerical studies [15–19] have been performed. With significant advancements in computational capabilities, numerical modeling has emerged as an increasingly efficient approach. In spite of traditional numerical methods, such as the level set method, volume-of-fluid method, and the lattice Boltzmann equation (LBE) method rooted in kinetic theory, a powerful tool for simulating contact-line dynamics due to its innate kinetic nature, excellent adaptability for parallel computing, and ease in dealing with irregular boundaries [20–22] has been developed. To date, numerous LBE models for multiphase flows have been developed based on diverse physical perspectives including the color-gradient model [23–25], the pseudopotential model [26–28], the free-energy model [29–31], and the phase-field-based model [32–34]. Compared with other models, the phase-field LBE model has attracted much attention due to its simplicity and accuracy. Since the total mass variation is managed by the interface tracking equation, implementation of the wetting boundary conditions for the phase distribution function in the phase-field LBE model becomes more straightforward.

Within the LBE method community, the wettability of the solid boundaries is typically characterized by contact angles. Wetting boundary schemes are required to dictate the phase distribution at boundary nodes and achieve the desired contact angles. According to a recent work proposed by Zhang *et al.* [35], the most-used wetting boundary treatments for phase-field LBE models can be categorized into three types. The first approach, developed by Martys and Chen [36] and later integrated into the phase-field LBE model by Iwahara *et al.* [37], utilizes an artificial solid density to simulate fluid-solid interactions, positing solids as a two-phase fluid mixture. This straightforward and prevalent wetting boundary scheme is particularly apt for curved boundaries and numerous successful porous-media flow studies have been conducted based on it. However, the biggest disadvantage of this type of wetting boundary treatment is that contact angle is not an input parameter, but has an implicit relationship with the solid density, which requires extra prenumerical simulations [35]. The second type of wetting boundary treatment developed by Ding and Spelt [38] is from the viewpoint of the geometrical relation. Compared with the first type of boundary treatment, this boundary scheme can be mathematically proved that the numerically imposed contact angle can be guaranteed to be the exact prescribed value explicitly. Many contributions have been made to implement this method based on phase-field LBE models and it has been successfully applied to the LBE method simulations of fluid-solid wetting phenomena [39–42]. The last type of wetting treatment was developed

---

*Corresponding author: bicheng.yan@kaust.edu.sa

†Corresponding author: shuyu.sun@kaust.edu.sa

by Briant [43,44]. Based on the surface-energy method, and Lee and Liu [45] extended this method into the phase-field LBE model. In this scheme, the driven force of the motion of contact line is the surface energy, which is regarded as part of the free energy of the system. The surface energy related to the gradient of the order parameter ϕ is considered as the wetting boundary condition, which can be expressed as $\kappa \boldsymbol{n}_w \cdot \nabla \phi = d\psi_s/d\phi$, where $\boldsymbol{n}_w$ is the normal vector pointing from solid to fluid, ψ_s represents the surface energy, and κ is the positive free-energy coefficient. Compared to the above two, this type of wetting boundary treatment can intuitively and accurately simulate a given contact angle with a solid physical foundation, so this work primarily focuses on this kind of boundary treatment.

In the original models, surface energy was defined as a linear function of the order parameter, which inadvertently introduced an undesirable mass layer [46]. To address this, recent adaptations have explored alternative functional representations for surface energy, including sine and cubic functions [47–49]. Taking the cubic form as an example, the wetting boundary condition can be expressed as $\boldsymbol{n}_w \cdot \nabla \phi = -\sqrt{2\beta/\kappa} \cos\theta(\phi - \phi^2)$, where β is a physical parameter determined by the given interface thickness and surface tension. In the calculation, the above boundary condition is actually adopted to determine the order parameters on the ghost solid node. Obviously, it is relatively easy to handle this for a flat boundary, where the normal vector $\boldsymbol{n}_w$ points to a given lattice node. The order parameter on the ghost cells can be obtained by solving the aforementioned quadratic equation, with the gradient term directly determined through interpolation. While for the curved boundaries, the calculation of order parameters at ghost cells is very complicated. To simplify the implementation, Connington and Lee [50,51] effectively assumed that the normal vector is in the direction along the lattice link, pointing away from the solid. This approach offers a degree of simplification in boundary handling, but it comes at the expense of computational accuracy. Apart from that, Fakhari and Bolster [52,53] adopted a biquadratic interpolation to determine the order parameter along the normal vector. Given its implicit nature, this method might necessitate iterative solutions. Although the authors introduced a simplified version in their studies, linear or quadratic interpolations are still required, and additional judgments for the normal vectors are required in the calculation, which complicates its implementation.

To the best of our knowledge, there remains a trade-off between implementation accuracy and complexity when dealing with the free-energy wetting boundary in the phase-field LB model. A boundary treatment with a clear physical basis, simple implementation, and good accuracy is still needed. To achieve this objective, a simplified implementation of the wetting boundary condition for Cahn-Hilliard (CH) based phase-field LBE method is proposed in this work. The

remainder of this paper is organized as follows. In Sec. II, the details of implementation for the wetting boundary condition are introduced after giving the governing equations and LBE method for two-phase flow. Section III provides the numerical validation to test the performance of the proposed boundary treatment. Finally, a summary is given in Sec. IV.

II. MATHEMATICAL METHOD

A. Governing equations and lattice Boltzmann method for two-phase flow

1. Governing equations

The two-phase incompressible fluid flows can be governed by the Navier-Stokes (NS) equations and the CH equation, which can be expressed as [54]

$$\nabla \cdot \boldsymbol{u} = 0, \tag{1a}$$

$$\partial_t(\rho \boldsymbol{u}) + \nabla \cdot (\rho \boldsymbol{u}\boldsymbol{u}) = -\nabla p + \nabla \cdot \left[\rho \nu (\nabla \boldsymbol{u} + \nabla \boldsymbol{u}^T)\right] + \boldsymbol{F}_s + \boldsymbol{F}_b, \tag{1b}$$

$$\partial_t \phi + \boldsymbol{u} \cdot \nabla \phi = \nabla \cdot (M \nabla \mu_\phi), \tag{1c}$$

where $\boldsymbol{u}$ is the velocity, ρ is the density, p is the pressure, and ν is the kinematic viscosity. $\boldsymbol{F}_s$ donates the surface tension force, which is chosen as $\boldsymbol{F}_s = \mu_\phi \nabla \phi$, with μ_ϕ being the chemical potential. $\boldsymbol{F}_b$ is the body force. ϕ represents the order parameter, which is used to distinguish the different phases. In this work, the order parameter is set as 1 and 0 for liquid and vapor phases, respectively, with a diffuse phase interface from 0 to 1. M represents the mobility.

In a two-phase system, the density and viscosity are no longer homogeneous as they exhibit discontinuities at the liquid-gas interface, which are all assumed to be linear functions of the order parameter here [55]

$$\rho = \phi(\rho_l - \rho_v) + \rho_v, \quad \nu = \phi(\nu_l - \nu_v) + \nu_v, \tag{2}$$

where the subscripts l and v represent the liquid phase and the vapor phase, respectively.

2. Lattice Boltzmann model for incompressible fluid flow

In the LBE method, the space is discretized into regular lattices and all particle distribution functions (PDF) are assumed to move with a series of discrete velocities on the nodes. In the standard LBE model, the evolution of these PDF can be described by [20]

$$f_i(\boldsymbol{x} + \boldsymbol{c}_i\delta_t, t + \delta_t) - f_i(\boldsymbol{x}, t) = -\frac{1}{\tau_f}\left[f_i(\boldsymbol{x}, t) - f_i^{\text{eq}}(\boldsymbol{x}, t)\right] + \delta_t F_i(\boldsymbol{x}, t), \tag{3}$$

where $f_i(\boldsymbol{x}, t)$ is the PDF at position $\boldsymbol{x}$ and time t. $\boldsymbol{c}_i$ is the discrete velocity. In two dimensions, the most popular two-dimension-nine-velocity (D2Q9) is adopted here, and $\boldsymbol{c}_i$ is defined as

$$\boldsymbol{c}_i = \begin{cases} (0,0)c, & i = 0, \\ (\cos[(i-2)\pi/2], \sin[(i-2)\pi/2])c, & i = 1 \sim 4, \\ \sqrt{2}(\cos[(i-5)\pi/2 + \pi/4], \sin[(i-5)\pi/2 + \pi/4])c, & i = 5 \sim 8, \end{cases} \tag{4}$$

where $c = \delta_x/\delta_t$ is the lattice speed with δ_x and δ_t being the lattice spacing and time step, respectively. In three dimensions, the three-dimension-nineteen-velocity (D3Q19) model is used in which the discrete velocity can be expressed as

$$
\boldsymbol{c}_i = \begin{cases} c(0,0,0), & i = 0, \\ c(\pm 1, 0, 0), c(0, \pm 1, 0), c(0, 0, \pm 1), & i = 1 \sim 6, \\ c(\pm 1, \pm 1, 0), c(\pm 1, 0, \pm 1), c(0, \pm 1, \pm 1), & i = 7 \sim 18. \end{cases} \tag{5}
$$

τ_f in Eq. (3) is the viscosity-related relation time. f_i^{eq} is the equilibrium distribution function, which can be written as

$$
f_i^{\text{eq}} = \begin{cases} \frac{p}{c_s^2}(\omega_i - 1) + \rho s_i(\boldsymbol{u}), & i = 0, \\ \frac{p}{c_s^2}\omega_i + \rho s_i(\boldsymbol{u}), & i \neq 0, \end{cases} \tag{6}
$$

with $s_i(\boldsymbol{u})$ being written as

$$
s_i(\boldsymbol{u}) = \omega_i \left[\frac{\boldsymbol{c}_i \cdot \boldsymbol{u}}{c_s^2} + \frac{(\boldsymbol{c}_i \cdot \boldsymbol{u})^2}{2c_s^4} - \frac{\boldsymbol{u} \cdot \boldsymbol{u}}{2c_s^2} \right], \tag{7}
$$

where ω_i is the weighting coefficient and c_s is the sound speed, which are defined as

$$
\omega_0 = \frac{4}{9}, \quad \omega_{1-4} = \frac{1}{9}, \quad \omega_{5-8} = \frac{1}{36}, \quad c_s^2 = \frac{c^2}{3}, \quad \text{for D2Q9,} \tag{8a}
$$

$$
\omega_0 = \frac{1}{3}, \quad \omega_{1-6} = \frac{1}{18}, \quad \omega_{7-18} = \frac{1}{36}, \quad c_s^2 = \frac{c^2}{3}, \quad \text{for D3Q19.} \tag{8b}
$$

$F_i(\boldsymbol{x}, t)$ in Eq. (3) symbolizes the force distribution function, which is elaborately designed as [56]

$$
F_i = \left(1 - \frac{1}{2\tau_g}\right) \omega_i \left[\boldsymbol{u} \cdot \nabla\rho + \frac{\boldsymbol{c}_i \cdot \boldsymbol{F}}{c_s^2} + \frac{\boldsymbol{u}\nabla\rho : (\boldsymbol{c}_i\boldsymbol{c}_i - c_s^2\boldsymbol{I})}{c_s^2} \right], \tag{9}
$$

where $\boldsymbol{F} = \boldsymbol{F}_s + \boldsymbol{F}_b$ is the total force. The fluid pressure and velocity in the present model can be calculated as

$$
p = \frac{c_s^2}{(1 - \omega_0)} \left[\sum_{i \neq 0} f_i + 0.5\delta_t \boldsymbol{u} \cdot \nabla\rho + \rho s_0(u) \right], \tag{10a}
$$

$$
\rho\boldsymbol{u} = \sum_i \boldsymbol{c}_i f_i + 0.5\delta_t \boldsymbol{F}, \tag{10b}
$$

Based on the Chapman-Enskog analysis [20], the NS equations can be recovered from Eq. (3) with the fluid kinematic viscosity determining by

$$
\nu = c_s^2(\tau_f - 0.5)\delta_t. \tag{11}
$$

3. Lattice Boltzmann model for phase interface capture

For the phase interface capture, the well-balanced LBE model is adopted here [57], in which the LB evolution equation with the BGK collision operator for the CH equation is expressed as

$$
g_i(\boldsymbol{x} + \boldsymbol{c}_i\delta_t, t + \delta_t) - g_i(\boldsymbol{x}, t)
$$
$$
= -\frac{1}{\tau_g} \left[g_i(\boldsymbol{x}, t) - g_i^{\text{eq}}(\boldsymbol{x}, t) \right]
$$
$$
+ \delta_t G_i(\boldsymbol{x}, t) + \frac{1}{2}\delta_t^2 \partial_t G_i(\boldsymbol{x}, t), \tag{12}
$$

where g_i is another set of PDFs used to describe the evolution of the phase interface, with the equilibrium distribution

function g_i^{eq} defined as

$$
g_i^{\text{eq}} = \begin{cases} \phi - (1 - \omega_0)\alpha\mu_\phi, & i = 0, \\ \omega_i\alpha\mu_\phi, & i \neq 0, \end{cases} \tag{13}
$$

where α is an adjusted parameter. The source term G_i is defined as

$$
G_i = \omega_i(\boldsymbol{u} \cdot \nabla\phi) \left[-1 + \frac{\boldsymbol{I} : (\boldsymbol{c}_i\boldsymbol{c}_i - c_s^2\boldsymbol{I})}{2c_s^2} \right], \tag{14}
$$

D2Q9 LBE model is adopted for two-dimensional calculations and three-dimension-seven-velocity (D3Q7) LBE model is used for three-dimensional simulations, which could reduce the computational cost without loss of accuracy. In D3Q7 model, the discrete velocity $\boldsymbol{c}_i$ is defined as

$$
\boldsymbol{c}_i = \begin{pmatrix} 0 & 1 & -1 & 0 & 0 & 0 & 0 \\ 0 & 0 & 0 & 1 & -1 & 0 & 0 \\ 0 & 0 & 0 & 0 & 0 & 1 & -1 \end{pmatrix}. \tag{15}
$$

The weighting coefficient and sound speed are defined as

$$
\omega_0 = \frac{1}{4}, \quad \omega_{1-6} = \frac{1}{8}, \quad c_s^2 = \frac{c^2}{4}. \tag{16}
$$

The order parameter in this model can be computed by

$$
\phi = \sum_i g_i. \tag{17}
$$

Applying the CE analysis to Eq. (12), the CH equation can be exactly recovered without any additional assumption, and the relation between the mobility M and the relation time τ_g can be expressed as

$$
M_\phi = c_s^2\alpha(\tau_g - 0.5)\delta_t. \tag{18}
$$

To achieve precise numerical computations, it's essential to employ suitable difference schemes when discretizing the

model's derivative terms. For simplicity, the gradient term can be determined using a second-order isotropic central scheme [55,58]

$$\nabla \Gamma(\boldsymbol{x}) = \sum_{i \neq 0} \frac{\omega_i \boldsymbol{c}_i \Gamma(\boldsymbol{x} + \boldsymbol{c}_i \delta_t)}{c_s^2 \delta_t}, \tag{19}$$

and the Laplace operator can be calculated by

$$\nabla^2 \Gamma(\boldsymbol{x}) = \sum_{i \neq 0} \frac{2\omega_i [\Gamma(\boldsymbol{x} + \boldsymbol{c}_i \delta_t) - \Gamma(\boldsymbol{x})]}{c_s^2 \delta_t^2}, \tag{20}$$

where Γ is the any physical variable.

B. Wetting boundary condition

1. Construction of the wetting boundary condition

When two-phase fluids come into contact with a solid substrate, the substrate's wettability significantly impacts fluid interface dynamics. Therefore, it is essential to establish a wetting boundary condition that incorporates the contact angle between the phase interface and the solid surface. In this subsection, we will give the details on the construction of the wetting boundary conditions, and propose a simplified implementation for it based on the above phase-field LBE model.

First, we denote a multiphase flow domain by Ω and its solid boundary by $\partial \Omega$, then the total free energy of this system can be expressed as [9,59,60]

$$\mathcal{F} = \int_{\Omega} \Psi(\phi, \nabla \phi) d\Omega$$
$$= \int_{\Omega} \left[\psi(\phi) + \frac{\kappa}{2} |\nabla \phi|^2 \right] d\Omega + \int_{\partial \Omega} \psi_s(\phi) ds, \tag{21}$$

where Ψ donates the total free-energy density and $\psi(\phi)$ is the bulk free-energy density which is chosen to have a double-well form [55] in this work

$$\psi(\phi) = \beta \phi^2 (\phi - 1)^2. \tag{22}$$

$\frac{\kappa}{2} |\nabla \phi|^2$ accounts for the phase-interface free energy density with κ being a positive free-energy coefficient and ψ_s is the free-energy density on the fluid-solid boundary. Applying the variational operator to Eq. (21), we can obtain

$$\delta \mathcal{F} = \int_{\Omega} \left[\frac{\partial \psi}{\partial \phi} \delta \phi + \kappa \nabla \phi \cdot \delta(\nabla \phi) \right] d\Omega + \int_{\partial \Omega} \frac{\partial \psi_s}{\partial \phi} \delta \phi ds, \tag{23}$$

which can be further written as follows by using the Gauss integral theorem [60]:

$$\delta \mathcal{F} = \int_{\Omega} \left[\frac{\partial \psi}{\partial \phi} - \kappa \nabla^2 \phi \right] \delta \phi d\Omega$$
$$+ \int_{\partial \Omega} \left[-\kappa \boldsymbol{n}_w \cdot \nabla \phi + \frac{\partial \psi_s}{\partial \phi} \right] \delta \phi ds. \tag{24}$$

Obviously, how to specify the wall free-energy density ψ_s is important. Similar to the existing studies, the cubic wall free energy is adopted with the interactions between solid and bulk phases neglected, and only the interaction at the three-phase

junction is considered [36,49]

$$\psi_s = \frac{b_1}{2} \phi^2 - \frac{b_1}{3} \phi^3, \tag{25}$$

then $\partial \psi_s / \partial \phi = b_1(\phi - \phi^2)$, with b_1 needing to be specified. Referring to Ref. [60], another constraint condition in the bulk region can be derived according to Eq. (24),

$$\frac{d\psi_s}{d\phi} = \pm \sqrt{2\kappa \psi}. \tag{26}$$

Combining Eqs. (22), (25), and (26), It can be found that Eq. (26) has two stable solutions of $\phi_{s1} = 0$ and $\phi_{s2} = 1$. Subsequently, the surface tensions of the gas-solid and liquid-solid phases can be represented as [61]

$$\sigma_{sg} = \frac{b_1}{2} \phi_{s1}^2 - \frac{b_1}{3} \phi_{s1}^3 + \int_0^{\phi_{s1}} \sqrt{2\kappa \psi} d\phi = 0, \tag{27a}$$

$$\sigma_{sl} = \frac{b_1}{2} \phi_{s2}^2 - \frac{b_1}{3} \phi_{s2}^3 + \int_1^{\phi_{s2}} \sqrt{2\kappa \psi} d\phi = \frac{b_1}{6}. \tag{27b}$$

Then, for the two-phase fluids on the chemically homogeneous wall, the contact angle can be determined based on the Young's equation [62]

$$\cos \theta = \frac{\sigma_{sg} - \sigma_{sl}}{\sigma} = -\frac{b_1}{\sqrt{2\kappa \beta}}. \tag{28}$$

According to Eqs. (25) and (28), the free-energy functional can be written as

$$\delta \mathcal{F} = \int_{\Omega} \left[\frac{\partial \psi}{\partial \phi} - \kappa \nabla^2 \phi \right] \delta \phi d\Omega$$
$$+ \int_{\partial \Omega} [-\kappa \boldsymbol{n}_w \cdot \nabla \phi - \sqrt{2\kappa \beta} \cos \theta (\phi - \phi^2)] \delta \phi ds, \tag{29}$$

where $\boldsymbol{n}_w$ is the normal vector pointing from solid to the fluid. In fact, by introducing the effective surface area, i.e., a_v, the surface integral in the above equation can be transformed into a volume integral [63], which can be expressed as

$$\delta \mathcal{F} = \int_{\Omega} \left[\frac{\partial \psi}{\partial \phi} - \kappa \nabla^2 \phi - a_v \kappa \boldsymbol{n}_w \cdot \nabla \phi \right.$$
$$\left. - a_v \sqrt{2\kappa \beta} \cos \theta (\phi - \phi^2) \right] \delta \phi d\Omega. \tag{30}$$

The variation of free energy $\mathcal{F}$ with regard to order parameter is referred to as the chemical potential [31]

$$\mu_\phi = \frac{d\psi}{d\phi} - \kappa \nabla^2 \phi - a_v [\kappa \boldsymbol{n}_w \cdot \nabla \phi + \sqrt{2\kappa \beta} \cos \theta (\phi - \phi^2)]. \tag{31}$$

The first two terms on the right-hand side of Eq. (31) represent the chemical potentials in the bulk area and at the phase interface. The third term represents that on the domain boundary $\partial \Omega$. Actually, Eq. (31) is usually implemented coupled with the boundary treatments

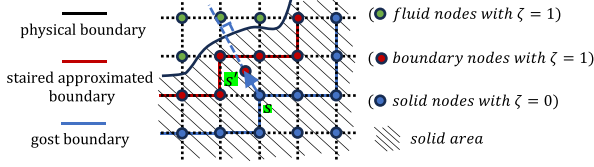$$\boldsymbol{n}_w \cdot \nabla \phi = \chi, \tag{32}$$

FIG. 1. Schematic illustration for the lattice nodes around the physical boundary.

with Eq. (31) being expressed as

$$\mu_\phi = \frac{d\psi}{d\phi} - \kappa\nabla^2\phi - a_v[\kappa\chi + \sqrt{2\kappa\beta}\cos\theta(\phi - \phi^2)], \quad (33)$$

where any expressions of χ can lead to the preset wetting conditions, which is proved numerically in the Appendix. If $\chi = -\sqrt{2\beta/\kappa}\cos\theta(\phi - \phi^2)$ is chosen, Eqs. (32) and (33) then becomes the usually used cubic wetting boundary condition. As discussed in the Introduction, it is complicated to implement the above boundary condition for the boundary with irregular geometry. To simplify the boundary treatment, we take $\chi = 0$ to switch Eq. (32) from the Robin boundary condition to the Neumann-type here

$$\boldsymbol{n}_w \cdot \boldsymbol{\nabla}\phi = 0. \quad (34)$$

Obviously, compared with the typical cubic wetting boundary condition, the implementation of Eq. (34) is much simpler. The chemical potential in a control volume then can be expressed as

$$\begin{aligned}\mu_\phi = {}& 4\beta\phi(\phi - 1)(\phi - 0.5) - \kappa\nabla^2\phi \\ & - a_v\sqrt{2\kappa\beta}\cos\theta(\phi - \phi^2).\end{aligned} \quad (35)$$

The combination of boundary condition [Eq. (34)] and chemical potential [Eq. (35)] can be used to describe the contact line motion of two-phase fluids.

2. Implementation of the boundary conditions

Figure 1 shows a two-dimensional schematic illustration for some lattice nodes near the boundary. A mark symbol ζ is introduced to distinguish the fluid ($\zeta = 1$)and solid ($\zeta = 0$) nodes. It is noted that the boundary nodes are marked as the same as the fluid nodes with $\zeta = 1$ due to the no-slip and no-flux boundary conditions are all implemented based on the modified bounce-back scheme in this work, where the boundary nodes also participate in the collision and streaming processes.

For the no-slip and no-flux boundary conditions, the unknown PDFs $f_i(\boldsymbol{x}_b)$ and $g_i(\boldsymbol{x}_b)$ can be calculated by the modified bounce-back scheme after the streaming step

$$f_i(\boldsymbol{x}_b) = f_{i'}(\boldsymbol{x}_b), \quad g_i(\boldsymbol{x}_b) = g_{i'}(\boldsymbol{x}_b), \quad (36)$$

where i' is the opposite direction of i. To capture the wetting phenomena, Eq. (34) should be used to determine the order parameter ϕ on the ghost lattice nodes. As shown in Fig. 1, $\phi(\boldsymbol{x}_s)$ should be equal to $\phi(\boldsymbol{x}_{s'})$, which is approximated by the average value of its surrounding nodes [35,64]

$$\phi(\boldsymbol{x}_s) = \phi(\boldsymbol{x}_{s'}) \approx \frac{\sum_i^b \zeta(\boldsymbol{x}_s + \boldsymbol{c}_i'\delta_t)\phi(\boldsymbol{x}_s + \boldsymbol{c}_i'\delta_t)}{\sum_i^b \zeta(\boldsymbol{x}_s + \boldsymbol{c}_i'\delta_t)}, \quad (37)$$
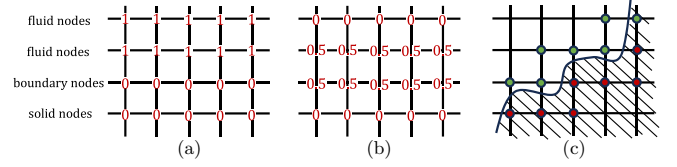

FIG. 2. Schematic illustration for (a) volume fraction ϵ, (b) the calculated effective surface area a_v/dx, and (c) lattice nodes involved in calculating the effective surface area of a curved boundary. The red dots represent boundary nodes and the green ones denotes fluid nodes.

where b is the total linked directions of a ghost node. For two-dimensional (2D) simulations, $b = 9$ and $\boldsymbol{c}_i' = \boldsymbol{c}_i$ in Eq. (4), but for three-dimensional (3D) cases, $b = 27$ and $\boldsymbol{c}_i'$ can be expressed as

$$\boldsymbol{c}' = (\boldsymbol{M} \ \boldsymbol{N}), \quad (38)$$

where $\boldsymbol{M}$ is the discrete velocity $\boldsymbol{c}_i$ in the D3Q19 model in Eq. (5) and $\boldsymbol{N}$ donates its supplement

$$\boldsymbol{N} = c\begin{pmatrix} 1 & -1 & 1 & -1 & 1 & -1 & 1 & -1 \\ 1 & 1 & -1 & -1 & 1 & 1 & -1 & -1 \\ 1 & 1 & 1 & 1 & -1 & -1 & -1 & -1 \end{pmatrix}. \quad (39)$$

3. Approximation of the effective surface area

In our proposed wetting boundary treatment, the effective surface area a_v is a crucial parameter, which is needed to be calculated with great care. For a flat boundary, the effective surface area is precisely equal to $1/\delta_x$. However, it is difficult to obtain its precise value for a solid boundary with irregular geometries and here we approximate it by [65,66]

$$a_v \approx |\boldsymbol{\nabla}\epsilon|. \quad (40)$$

The above equation starts from the volume averaging theorem, which links the porosity gradient to the average surface normal within a control volume, i,e., $-\boldsymbol{\nabla}\epsilon = (1/V)\int_{\partial_V} \boldsymbol{n}_w dA$. ϵ is the volume fraction of void space within a control volume, which is defined as

$$\epsilon = \begin{cases} 1, & \text{fluid nodes,} \\ 0, & \text{boundary nodes and solid nodes.} \end{cases} \quad (41)$$

It should be noted that ϵ at boundary nodes is set as zero, which is different with ζ. The gradient of ϵ can be calculated by Eq. (19). However, there is a sharp transition between the fluid region and the solid region, As shown in Figs. 2(a) and 2(b), Eq. (19) actually extends the wetting boundary effects to the adjacent fluid nodes. This two-layer's structure can ensure better accuracy when dealing with curved boundaries with the stair-step approximation. As shown in Fig. 2(c), the lattice nodes in the solid phase (marked as red dot) usually used to approximate the curved boundary, obviously, this approximation will extend the actual physical boundary towards the solid phase region which could introduce significant deviations. However, the structure of the double-layer surface chemical potential could naturally involve nearby fluid points (marked as the green dot), and lattice nodes on both sides of the
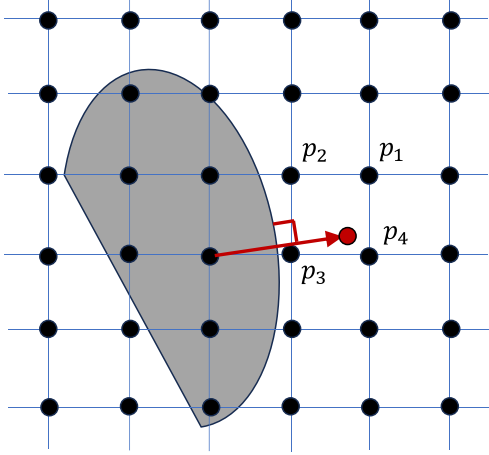
FIG. 3. Schematic illustration for the calculation of the gradient of order parameter along the boundary normal direction.

FIG. 4. Schematic illustration for the wetting of a droplet on an idea flat surface.

III. NUMERICAL TEST AND DISCUSSIONS

In this section, several benchmark examples including the droplet spreading on both flat, inclined, and curved ideal walls, are going to be performed to validate the accuracy of our proposed wetting boundary treatments.

A. Droplet spreading on the flat ideal wall

A fundamental two-phase droplet spreading problem on an ideal wall is initially employed to validate the capability of the established numerical approach in predicting the wide range of contact angles. The simulations are performed in $Nx \times Ny = 256 \times 128$ rectangular domain for 2D simulations. A semicircular droplet with the radius $R = 50$ is initially deposited on the flat solid wall. The thickness of the solid plate is $0.25Ny$, which is $0.05Ny$ from the bottom (as displayed in Fig. 4). It is noted that for very low contact angles of $\theta = 20°$ and $10°$, the steady droplet has exceeded the grid space, and then we decrease the radius of the droplet to $R = 40$ and 30, respectively. To match this setup, the initial distribution profile of the order parameter is given by [67]

$$\phi(x, y) = 0.5 + 0.5 \tanh \frac{2[R - \sqrt{(x - x_0)^2 + (y - y_0)^2}]}{W}.$$
(42)

The analytical solution of the order parameter for the droplet at the equilibrium state can be expressed as

$$\phi_r = 0.5 + 0.5 \tanh \frac{2[R_r - \sqrt{(x - x_r)^2 + (y - y_r)^2}]}{W}, \quad (43)$$

where $R_r = L_r / \sin(\theta)$, $x_r = x_0$, and $y_r = y_0 - R_r \cos\theta$. During the simulations, some physical parameters are set as

4. Discussion for the advantage of the proposed new approach

From the above derivation, it becomes evident that the greatest advantage of our scheme is its ability to simplify the path to achieving wettability of boundaries with complex geometric shapes, while still ensuring calculation accuracy.

For the implementation of commonly used cubic wetting boundary condition, i.e., $\boldsymbol{n}_w \cdot \nabla\phi = -\sqrt{2\beta/\kappa} \cos\theta(\phi - \phi^2)$, it is essential to ensure the accuracy of solving the normal gradient on the left-hand side of this boundary equation. As shown in Fig. 3, the most straightforward approach involves determining a point along the normal vector of the surface for a ghost grid with unknown order parameters. However, it's not guaranteed that this point falls precisely on the grid. Therefore, we typically require the grid points around it to approximate and obtain the order parameter value at that point. Finally, the normal gradient is expressed as a function of the ghost grid order parameter through the finite difference method. Combined with the cubic wetting boundary condition, the order parameter on the ghost grid can be obtained. This process is relatively complicated to implement in the program, and numerical instability may occur for some cases with complex media structures.

However, in our proposed method, the above cubic wetting boundary condition is calculated explicitly in the chemical potential, and only Neumann-type boundary condition [Eq. (34)] needs to be implemented, where the unknown order parameter on a ghost grid can be approximated by the average value of its surrounding nodes [Eq. (37)]. Compared with the original scheme, this greatly simplifies the implementation process, and numerical results show that it can also ensure high accuracy, which will be discussed in the next section.
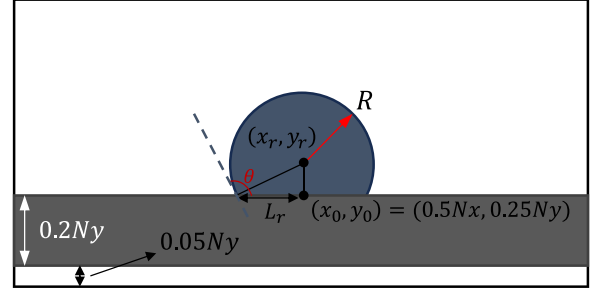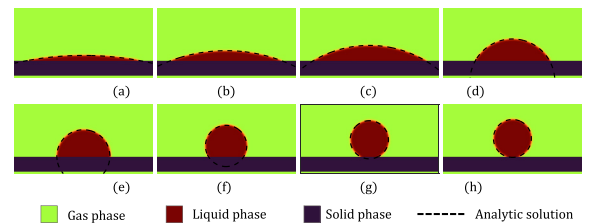

FIG. 5. The predicted droplet equilibrium shapes in 2D using the present boundary treatment with wide range of prescribed contact angles, (a) $\theta = 10°$, (b) $\theta = 20°$, (c) $\theta = 30°$, (d) $\theta = 60°$, (e) $\theta = 90°$, (f) $\theta = 120°$, (g) $\theta = 150°$, and (h) $\theta = 160°$.

TABLE I. Simulation results of the proposed wetting schemes in predicting wide range of contact angles.

Contact angle (°)	2D results (°)	3D results (°)	2D errors (°)	3D errors (°)
10	10.2	12.3	0.2	2.3
20	19.3	19.7	0.7	0.3
30	29.6	30.2	0.4	0.2
40	39.2	39.7	0.8	0.3
60	59.3	59.5	0.7	0.5
90	89.5	89.9	0.5	0.1
120	119.9	120.7	0.1	0.7
140	140.2	142.8	0.2	2.8
150	150.1	156.3	0.2	6.3
160	159.7	180	0.3	–
170	168.3	180	1.7	–

$\rho_l = 10.0$, $\rho_g = 1.0$, $v_l = v_g = 0.1$, $\sigma = 0.005$, $M = 0.01$, and $W = 4$. The periodic boundary condition is applied at all surrounding boundaries, and the wetting boundary treatments are adopted for the fluid-solid interface. Figure 5 illustrates the droplet equilibrium shapes predicted by the LBE method, incorporating the proposed surface energy wetting boundary treatment across a broad spectrum of specified contact angles. As evident from Fig. 5, the droplet can assume various stable configurations on the substrate, which are significantly influenced by the specified contact angle, and the numerical results all agree well with the analytical solutions.

Table I summarizes the quantitative comparison between the given contact angles and the numerically obtained ones. It reveals that the current wetting boundary treatments are able to obtain satisfactory results for the entire range of contact angles from 10° to 160° for 2D simulations, with the maximum absolute errors generally falling below 1°. A contact angle above 150° indicates superhydrophobic wetting properties. Numerically modeling the contact angle within such wetting regions poses challenges due to significant interface deformation, which can potentially lead to numerical instability. However, it is shown that the predicted values are overall consistent with the prescribed one, even when for the case
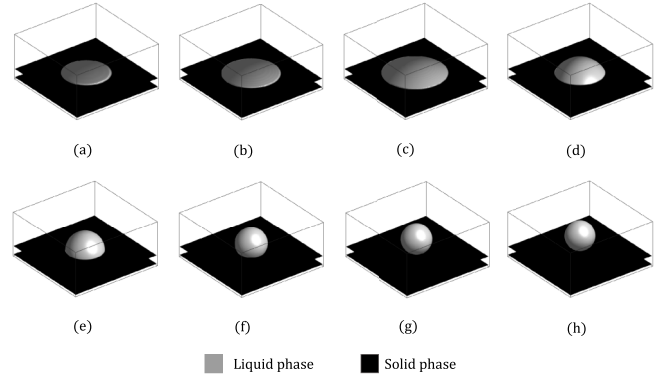

FIG. 7. The predicted droplet equilibrium shapes in three dimensions using the present boundary treatment with wide range of prescribed contact angles (a) $\theta = 10°$, (b) $\theta = 20°$, (c) $\theta = 30°$, (d) $\theta = 60°$, (e) $\theta = 90°$, (f) $\theta = 120°$, (g) $\theta = 150°$, and (h) $\theta = 160°$.

with contact angle $\theta = 170°$, the absolute error is also less than 2°, which proves the good performance of the present scheme.

We further computed and plotted the velocity field at different contact angles in Fig. 6 to further confirm whether the spurious velocity at steady state will affect the simulation results. As can be observed, the maximum velocity for the wetting problem on a two-dimensional flat plate is of the order of 10^{-6}, which is regarded as negligible in most scenarios.

In the 3D testing cases, the initial conditions and parameter settings are basically consistent with those of the 2D scenario. The simulations are performed in $Nx \times Ny \times Nz = 256 \times 256 \times 128$ domain. The initial distribution profile of the order parameter is given by

$$\phi(x, y, z) = 0.5 + 0.5 \tanh$$

$$\times \frac{2[R - \sqrt{(x - x_0)^2 + (y - y_0)^2 + (z - z_0)^2}]}{W},$$

$$(44)$$

where $x_0 = 0.5Nx$, $y_0 = 0.5Ny$, and $z_0 = 0.25Nz$. Figure 7 depicts the 3D equilibrium shapes of the droplet at differ-

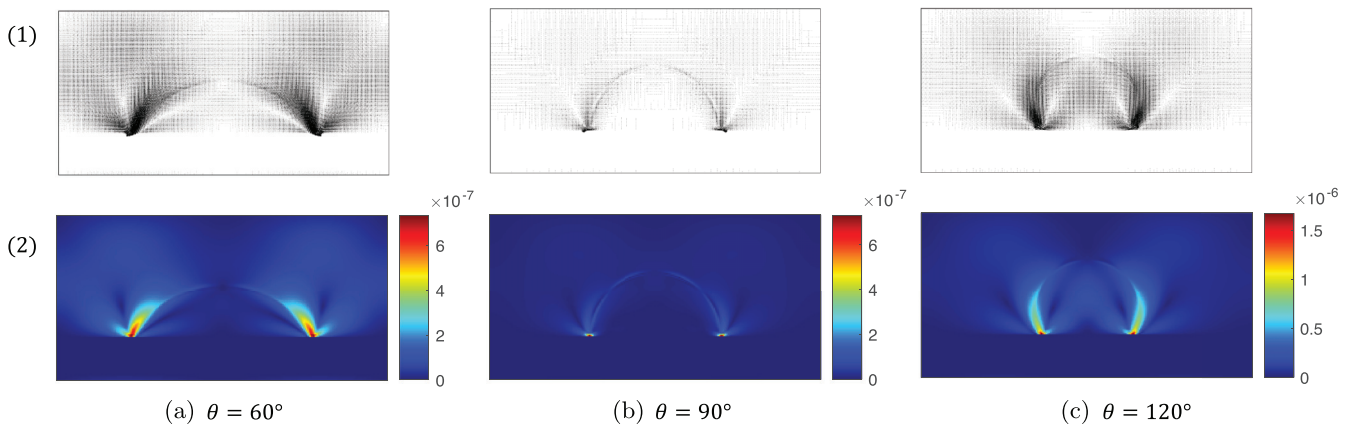(a) $\theta = 60°$ (b) $\theta = 90°$ (c) $\theta = 120°$

FIG. 6. Equilibrium velocity field for the cases of two-dimensional droplet spreading on the flat ideal wall. (1) Speed vector illustration and (2) Contour plot of velocity $|\boldsymbol{u}|$.
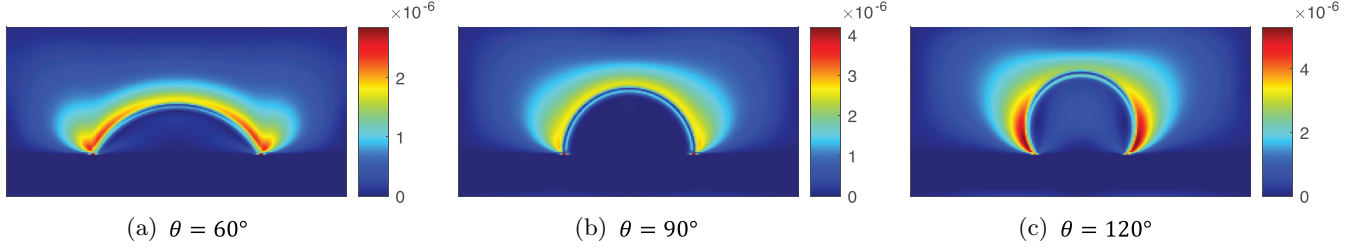
(a) $\theta = 60°$ (b) $\theta = 90°$ (c) $\theta = 120°$

FIG. 8. Contour plot of velocity $|\boldsymbol{u}|$ at equilibrium state for the cases of three-dimensional droplet spreading on the flat ideal wall.

ent wetting angles, and Table I presents the corresponding computed contact angles. From Table I, we can find that the present scheme is able to obtain satisfactory results for the entire range of contact angles from $10°$ to $140°$, of which the maximum absolute errors are almost less than $3°$. However, for the superhydrophobic wetting condition, the present boundary treatment works with poor performance, especially for the cases with $\theta = 160°$ and $170°$, where the droplets could be detached from the solid substrate, leading to a large prediction error. Compared to the 2D results, the 3D cases exhibit poorer performance in predicting superhydrophobic wetting. This can be attributed to the smaller contact area in 3D cases compared to 2D cases, where the contact line essentially acts as a contact surface of infinite length in the third dimension. This is considerably larger than the contact area in the 3D cases, which gradually reduces to a contact point as the wetting angle increases. Its inability to provide sufficient adhesion finally leads to the detachment of the droplet [60]. Figure 8 shows the contour plots of velocity $|\boldsymbol{u}|$ at the equilibrium state with different contact angles, and it can be seen that the maximum velocity for three-dimensional cases is on the order of $O(10^{-6})$.

B. Droplet spreading on the inclined ideal surface

To demonstrate the applicability of the present wetting boundary treatment for problems with more general geometries, testing cases, where droplets spread on the inclined ideal surface with different inclination angles are performed. The 2D configuration of the problem is shown in Fig. 9. As shown in this figure, an inclined solid is placed in the $Nx \times Ny = 256 \times 256$ rectangular domain for 2D simulations, with its slanted edge represented by $y = \tan(\gamma)x$, where γ is
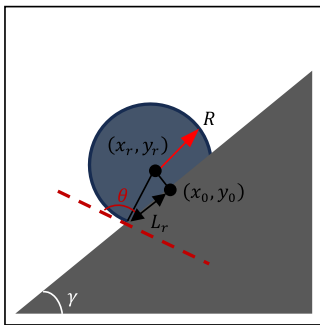
the inclination angle, and it is selected as $\gamma = \arctan(1.0)$, $\arctan(0.5)$, and $\arctan(0.25)$ to assess the accuracy of the proposed method. Initially, a semicircular droplet with radius of $R = 50$ is placed on the inclined surface, and the order parameter can be described by Eq. (42), with $(x_0, y_0) = [0.5N_x, \tan(\gamma)0.5N_x]$. Some parameters in the testing cases are set as $\rho_l = 10.0$, $\rho_g = 1.0$, $\nu_l = \nu_g = 0.1$, $\sigma = 0.005$, and $M = 0.01$, and the wetting boundary treatments are adopted for the fluid-solid interface. For 2D cases, the interface thickness is set as $W = 4$.

Figure 10 shows the simulation results with different wall inclination angles for different contact angles from $\theta = 30°$ to $150°$. For $\gamma = \arctan(1)$ and $\arctan(0.5)$, it can be seen that the numerical results agree well with the reference solutions, which are a set of circles with specific contact angles on the wetting surface obtained from geometric relationships. However, for the cases with $\gamma = \arctan(0.25)$, there are noticeable discrepancies between the numerical results and the reference solution when $\theta = 90°$ and $120°$. This discrepancy arises from the stair-stepped grid approximation for the inclined surface. A smaller inclination angle of the wall results in an elongated horizontal platform (as shown in Fig. 11). In certain scenarios, the triphase contact point may be located on this platform, leading to a deviation in the prediction of the contact angle. To validate this perspective, an increased interface thickness $W = 6$ and 8 were adopted to ensure that the three-phase contact region encompasses a broader extent of solid grid

(1) $\theta = 30°$ (2) $\theta = 60°$ (3) $\theta = 90°$ (4) $\theta = 120°$ (5) $\theta = 150°$

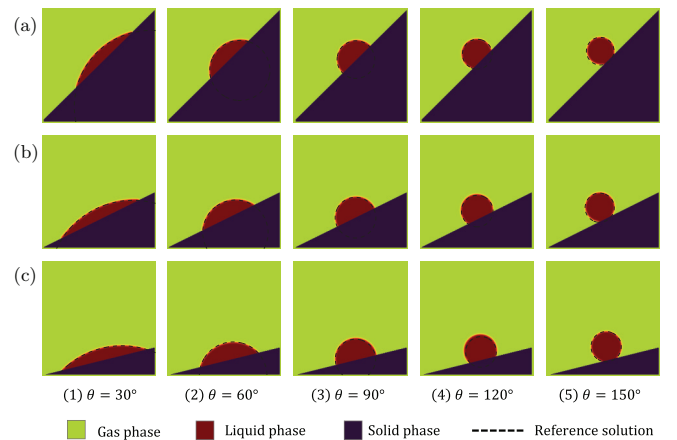Gas phase   Liquid phase   Solid phase   ------ Reference solution

FIG. 10. The predicted droplet equilibrium shapes on the inclined surface in two dimensions using the present boundary treatment with wide range of prescribed contact angles and different inclined angles γ, (a) $\gamma = \arctan(1.0)$, (b) $\gamma = \arctan(0.5)$, (c) $\gamma = \arctan(0.25)$.

FIG. 9. Schematic illustration for the wetting of a droplet on an idea inclined surface, θ is the contact angle, γ represents the inclined angle of the solid boundary.
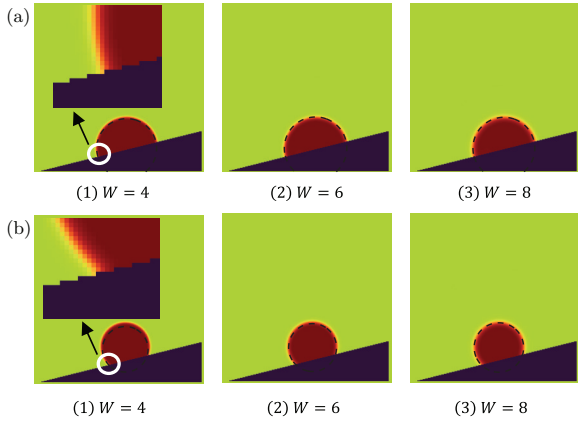
FIG. 11. The predicted droplet equilibrium shapes in two dimensions using the wetting boundary treatment with different width of phase interface W; contact angle (a) $\theta = 90°$ and (b) $\theta = 120°$.
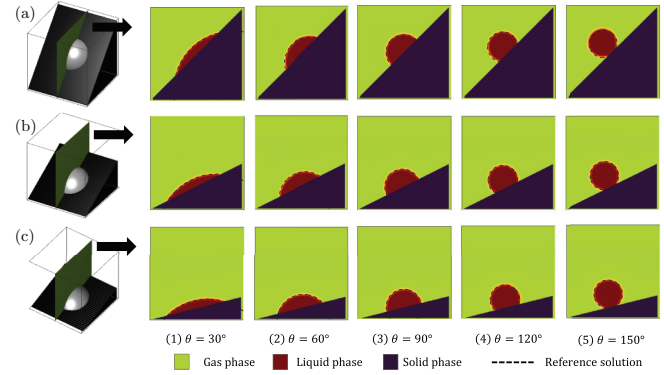

FIG. 13. The predicted droplet equilibrium shapes on the inclined surface in three dimensions using the present boundary treatment with wide range of prescribed contact angles and different inclined angles γ, (a) $\gamma = \arctan(1.0)$, (b) $\gamma = \arctan(0.5)$, (c) $\gamma = \arctan(0.25)$.

points, thereby enhancing the accuracy of the stair-stepped approximation. Figure 11 shows the numerical results for wetting angles of 90° and 120° with interface thicknesses $W = 6$ and 8. As observed, the alignment between the calculated and reference results improves with increasing interface thickness. These numerical findings substantiate the accuracy of the proposed scheme in 2D scenarios.

The velocity fields at equilibrium state with different contact angles and inclined angles in these two-dimensional cases are plotted in Fig. 12. It can be seen that for the cases, where the solid boundary aligns with the lattice link [$\gamma = \arctan(1)$], the spurious velocity is the smallest, on the order of 10^{-7}, while for the cases with a zig-zag approximated solid boundary, the spurious velocities are significantly larger,

but overall the maximum spurious velocity is still of the order of 10^{-5}.

For the 3D validation, the simulations are performed in the $Nx \times Ny \times Nz = 256 \times 256 \times 256$ domain. The slanted edge of the solid can be represented by $z = \tan(\gamma)x$. A droplet, shaped as a semicircle with a radius of $R = 50$, is positioned on the tilted surface with its center located at $(x_0, y_0, z_0) = [0.5N_x, 0.5N_y, \tan(\gamma)0.5N_x]$. Aside from setting the interface thickness to $W = 6$, all other parameters remain consistent with the two-dimensional setup. Figure 13 shows a comparison between the numerical solution and the reference solution. It can be observed that for various inclinations of the inclined surface, the wetting boundary treatment proposed in this study accurately predicts the
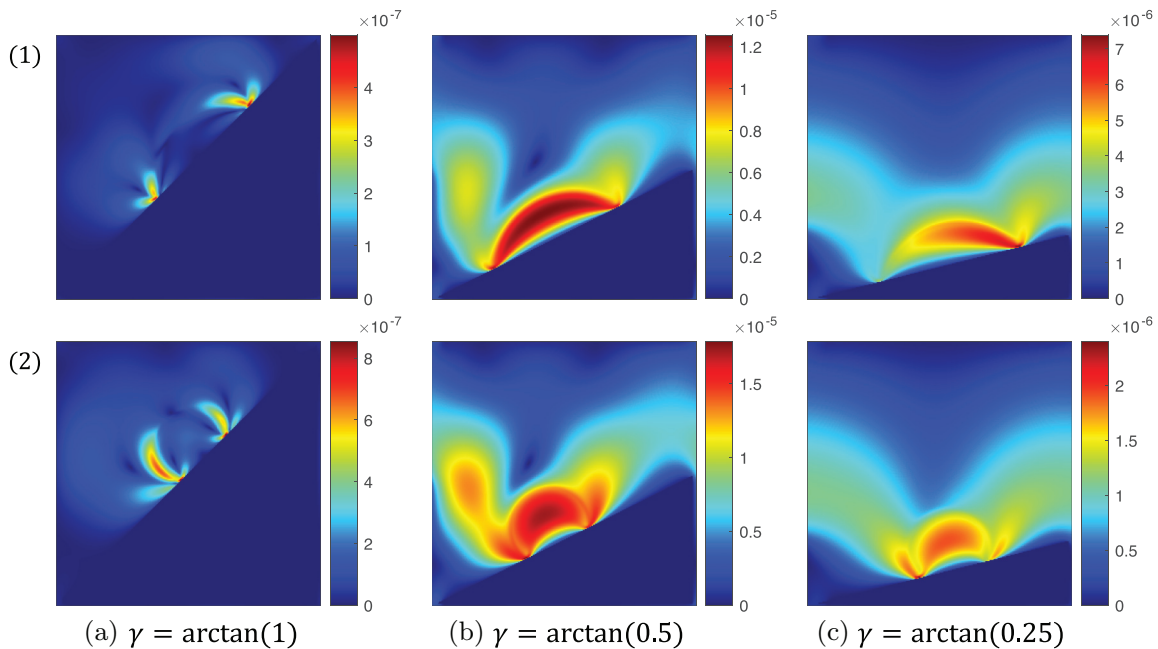

FIG. 12. Contour plot of velocity $|\mathbf{u}|$ at equilibrium state for the cases of two-dimensional droplet spreading on the inclined ideal wall. (1) Contact angle $\theta = 60°$, (2) contact angle $\theta = 120°$.
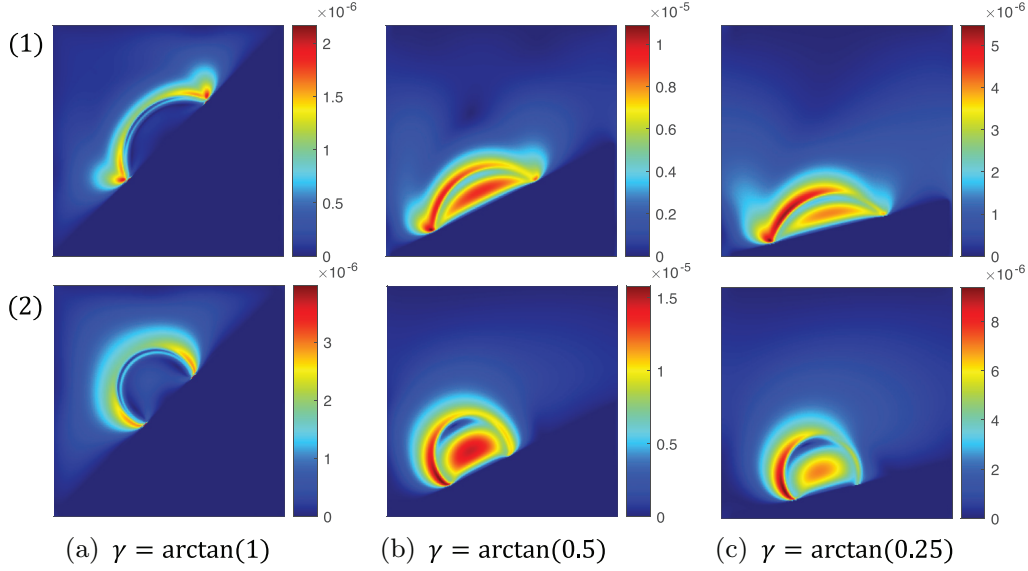
FIG. 14. Contour plot of velocity $|\boldsymbol{u}|$ at equilibrium state for the cases of three-dimensional droplet spreading on the inclined ideal wall. (1) contact angle $\theta = 60°$, (2) contact angle $\theta = 120°$.

wetting angle. The numerical solution aligns closely with the reference solution, demonstrating the capability of the proposed method for addressing three-dimensional wetting problems.

Figure 14 shows the velocity fields at equilibrium state with different contact angles in three-dimensional cases. Similar with those in two-dimensional cases, the maximum velocity is on the order of $O(10^{-5})$, which has negligible effects on the accuracy of the simulating results.

C. Droplet spreading on the cylindrical and sphere surface

In the above subsections, the performance of the proposed boundary treatment on flat walls has been proven, including both scenarios where the physical boundary aligns with the lattice link or not. In this subsection, the accuracy of the present model to enforce a designated contact angle on a curved boundary will be validated using the equilibrium configuration of a stationary droplet on a 2D circular surface and a 3D sphere.

For 2D simulations, a circular solid with a radius of $R_s = 60$ and the center located at $(x_s, y_s) = (0.5N_x, 0.5N_y - 50)$ is placed within a rectangular area of size $N_x \times N_y = 256 \times 256$. Initially, a droplet with a radius of $R_i = 50$ is placed on the surface of the solid, and the initial order parameter can be expressed as follows:

$$\phi(x, y) = 0.5 + 0.5 \tanh \frac{2[R_i - \sqrt{(x - x_0)^2 + (y - y_0)^2}]}{W},$$

$$(45)$$

where $(x_0, y_0) = (0.5N_x, 0.5N_y)$ is the initial center location of the droplet. At equilibrium, the free energy of the system minimizes, suggesting an inherent tendency for the droplet to assume a circular form. Figure 15 illustrates this equilibrium configuration of a droplet resting on a circular surface, and the

reference solution can be expressed as

$$\phi_f(x, y) = 0.5 + 0.5 \tanh \frac{2[R - \sqrt{(x - x_e)^2 + (y - y_e)^2}]}{W},$$

$$(46)$$

where $R = L / \cos \theta'$ is the radius of the equilibrium droplet. L can be obtained from the numerical solution and $\theta' = \theta - \theta^*$ with $\theta^* = \arccos(L/R_s)$. (x_e, y_e) is the center location of the equilibrium droplet, where $x_e = x_s$ and $y_e = y_s + \sqrt{R^2 + R_s^2 - 2RR_s \cos \theta}$. Parameters in simulations in these testing cases are set as $\rho_l = 10.0$, $\rho_g = 1.0$, $\nu_l = \nu_g = 0.1$, $\sigma = 0.005$, $M = 0.01$, and $W = 6$.

Figure 16 shows the comparison between the numerical results and the reference solutions for contact angles ranging from $30°$ to $150°$. As we can see, the numerical results agree well with the reference solutions, which proves the good performance of the proposed boundary treatment for 2D curved walls. The velocity field with different contact angles are shown in Fig. 17. As can be observed, the maximum velocity for the wetting problem on a two-dimensional on the
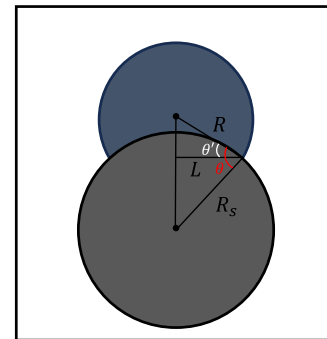

FIG. 15. Schematic illustration for the wetting of a droplet on a cylindrical solid, θ is the contact angle.

(a) $\theta = 30°$ (b) $\theta = 60°$ (c) $\theta = 90°$ (d) $\theta = 120°$ (e) $\theta = 150°$

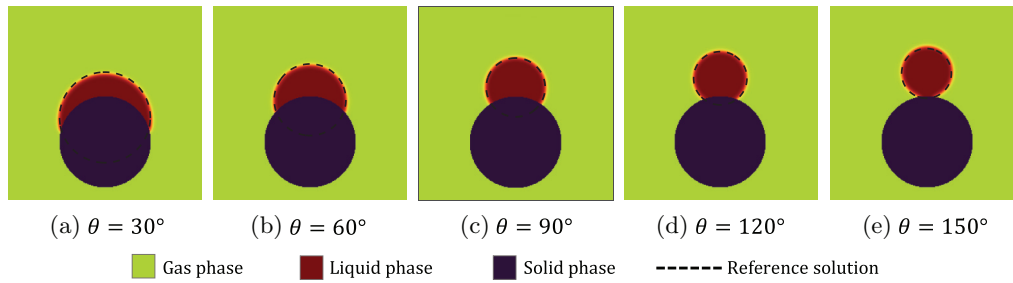Gas phase   Liquid phase   Solid phase   ------ Reference solution

FIG. 16. The predicted droplet equilibrium shapes on the cylindrical solid in two dimensions using the present boundary treatment with wide range of prescribed contact angles.

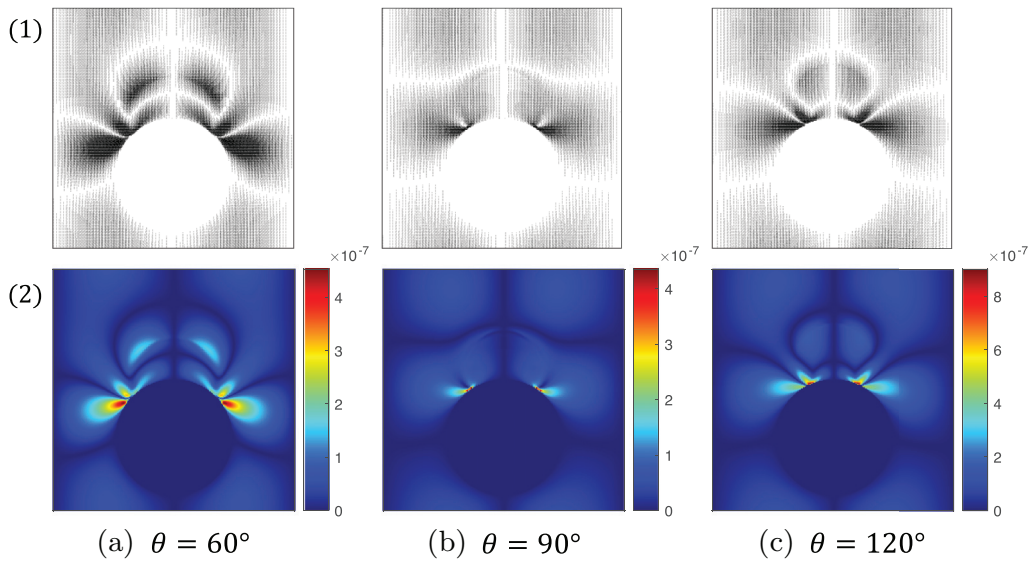(a) $\theta = 60°$ (b) $\theta = 90°$ (c) $\theta = 120°$

FIG. 17. Equilibrium velocity field for the cases of two-dimensional droplet spreading on the cylindrical surface. (1) Speed vector illustration and (2) Contour plot of velocity $|\boldsymbol{u}|$.

(a) $\theta = 30°$ (b) $\theta = 60°$ (c) $\theta = 90°$ (d) $\theta = 120°$ (e) $\theta = 150°$

Gas phase   Liquid phase   Solid phase   ------ Reference solution
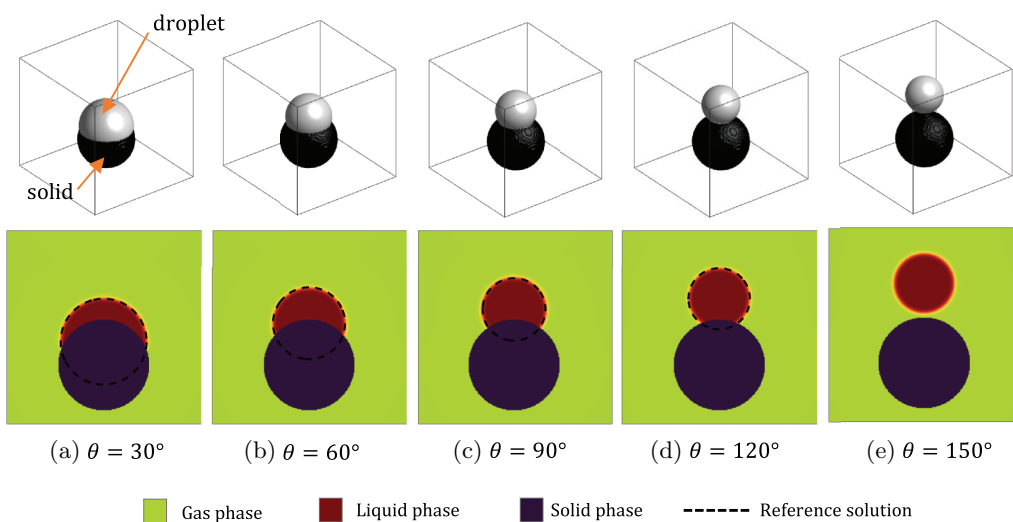
FIG. 18. The predicted droplet equilibrium shapes on a 3D solid sphere using the present boundary treatment with wide range of prescribed contact angles. The first row shows the 3D wetting morphology of the droplet, and the second row provides the distribution of order parameters in the central cross section, along with a comparison to the reference solution.
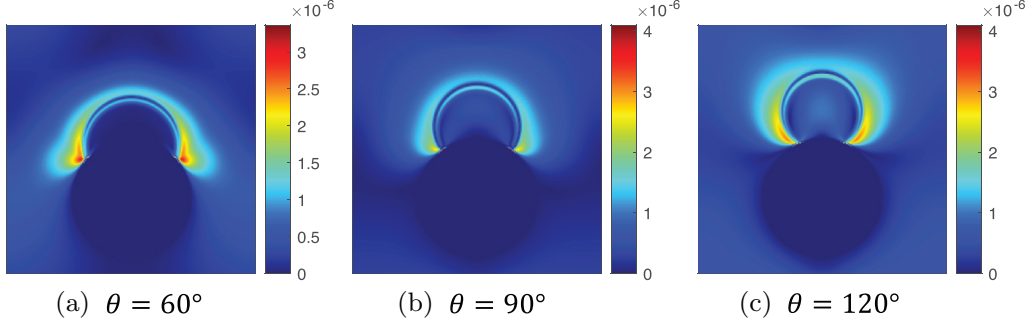
(a) $\theta = 60°$ (b) $\theta = 90°$ (c) $\theta = 120°$

FIG. 19. Contour plot of velocity $|\boldsymbol{u}|$ at equilibrium state for the cases of three-dimensional droplet spreading on the phere surface.

cylindrical surface is of the order of 10^{-7}. For 3D testing cases, the computational domain is $N_x \times N_y \times N_z = 256 \times 256 \times 256$, and the initial distribution of the order parameter can be expressed as

$$\phi(x, y, z) = 0.5 + 0.5 \tanh$$
$$\times \frac{2[R_i - \sqrt{(x - x_0)^2 + (y - y_0)^2 + (z - z_0)^2}]}{W}.$$
(47)

All the other simulation and geometrical parameters are set as the same as those in 2D cases. Figure 18 displays the 3D wetting morphology of the droplet at equilibrium, along with the phase-field distribution on the cross section at $y = 0.5N_y$ and its corresponding reference solution. From the figure, it can be observed that when the contact angle is less than $150°$, the numerical results agree well with the reference solutions. However, for the case with the designated contact angle $\theta = 150°$, the present boundary treatment works with poor performance. This serious deviation may be attributed to the fact that the droplet achieves a small wetting area on the sphere, as a result, the droplet could be detached from the solid substrate, which is similar to the testing cases on the flat wetting boundary, as is discussed in the above subsection. The velocity field in these three-dimensional cases are shown in Fig. 19. As can be observed, the maximum velocity for the wetting problem is of the order of 10^{-6}.

IV. CONCLUSION

In the present work, a simplified method is proposed to implement the free-energy-based wetting boundary condition based on the phase-field LBE method. The two-phase flow behavior is described by a well-balanced LBE model, and the wetting phenomena are governed by surface free energy. Taking the example of surface-free energy in cubic form, the proposed approach incorporates a portion of the surface-free energy into the chemical potential. Unlike previous methods that traditionally treated it as a boundary condition, the proposed approach only requires handling the boundary condition with zero gradients of the order parameter in the normal direction on the solid nodes, which can be approximated by the average value of the surrounding nodes. This approach significantly simplifies the implementation complexity of the wetting boundary condition. Several benchmark testing cases, including the 2D and 3D droplet spreading processes on flat, inclined, and curved ideal walls, were carried out to validate the accuracy of the proposed scheme. The results indicate the good ability and satisfactory accuracy of the proposed schemes to simulate wetting phenomena on curved boundaries, showing the application potential in the filed of oil recovery, carbon sequestration, soft matter, and active matter [68–71]. The boundary treatment proposed in this paper provides a simple and effective tool for the numerical simulations of phase behavior in the above potential research directions.

The data that support the findings of this study are available from the corresponding author upon reasonable request.

TABLE II. Selection of chemical potential μ_ϕ and χ in different cases.

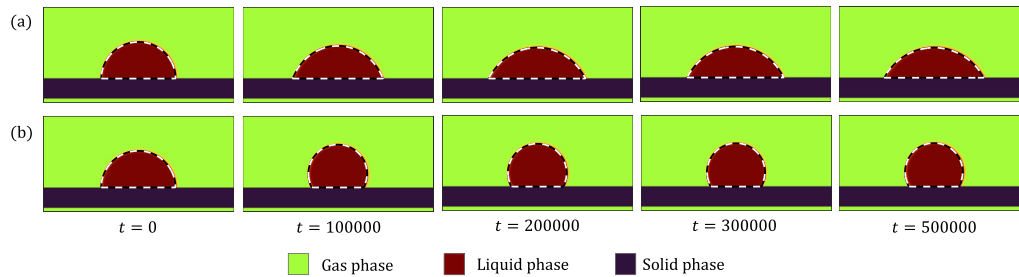|	χ	Chemical potential μ_ϕ
Case 1	$-\sqrt{2\beta/\kappa} \cos\theta(\phi - \phi^2)$	$\frac{d\psi}{d\phi} - \kappa\nabla^2\phi$
Case 2	0	$\frac{d\psi}{d\phi} - \kappa\nabla^2\phi - a_v[\sqrt{2\kappa\beta} \cos\theta(\phi - \phi^2)]$
Case 3	$\sqrt{2\beta/\kappa} \cos\theta(\phi - \phi^2)$	$\frac{d\psi}{d\phi} - \kappa\nabla^2\phi - 2a_v[\sqrt{2\kappa\beta} \cos\theta(\phi - \phi^2)]$

FIG. 20. Time evolution of the droplet spreading shapes with different contact angles, (a) $\theta = 60°$, (b) $\theta = 120°$. The results of case 1 with $\chi = -\sqrt{2\beta/\kappa}\cos\theta(\phi - \phi^2)$ are shown with color figure. The contours with $\phi = 0.5$ of case 2 and case 3 are marked with black line and white dashed line, respectively.

APPENDIX: NUMERICAL VERIFICATION OF THE IRRELEVANCE OF χ TO THE RESULTS

In this Appendix, we want to numerically prove that it is equivalent to treat the wall-free energy at the boundary condition or to embody it in the chemical potential. Thus, three different groups of chemical potential, μ_ϕ and χ are chosen to be the testing cases, which are listed in Table II.

To facilitate the calculation of cases 1 and 3, we selected the spreading process of droplets on an ideal horizontal plane as the test. The physical design and numerical parameters of the test are all consistent with those in Sec. III A. Figure 20 shows the time evolution of the droplet spreading shapes obtained by different cases. It can be clearly seen that at different contact angles, the results obtained at different times by different combinations of μ_ϕ and χ are consistent, which proves the irrelevance of χ to the wetting boundary treatment.

[1] V. Alvarado and E. Manrique, Enhanced oil recovery: An update review, Energies **3**, 1529 (2010).

[2] B. Yan, L. Mi, Y. Wang, H. Tang, C. An, and J. E. Killough, Multi-porosity multi-physics compositional simulation for gas storage and transport in highly heterogeneous shales, J. Pet. Sci. Engg. **160**, 498 (2018).

[3] D. Zhang and J. Song, Mechanisms for geological carbon sequestration, Procedia IUTAM **10**, 319 (2014).

[4] D. J. DePaolo and D. R. Cole, Geochemistry of geologic carbon sequestration: an overview, Rev. Mineral. Geochem. **77**, 1 (2013).

[5] Z. Tariq, E. U. Yildirim, M. Gudala, B. Yan, S. Sun, and H. Hoteit, Spatial–temporal prediction of minerals dissolution and precipitation using deep learning techniques: An implication to geological carbon sequestration, Fuel **341**, 127677 (2023).

[6] B. Yan, M. Gudala, and S. Sun, Robust optimization of geothermal recovery based on a generalized thermal decline model and deep learning, Energy Convers. Manage. **286**, 117033 (2023).

[7] T. Huang, G. J. Moridis, T. A. Blasingame, A. M. Abdulkader, and B. Yan, Compositional reservoir simulation of underground hydrogen storage in depleted gas reservoirs, Int. J. Hydrogen Energy **48**, 36035 (2023).

[8] R. Song, S. Sun, J. Liu, and C. Yang, Pore scale modeling on dissociation and transportation of methane hydrate in porous sediments, Energy **237**, 121630 (2021).

[9] P. G. de Gennes and G. Pierre, Wetting: statics and dynamics, Rev. Mod. Phys. **57**, 827 (1985).

[10] R. Cox, The dynamics of the spreading of liquids on a solid surface. part 1. viscous flow, J. Fluid Mech. **168**, 169 (1986).

[11] R. Cox, The dynamics of the spreading of liquids on a solid surface. part 2. surfactants, J. Fluid Mech. **168**, 195 (1986).

[12] H. Zhang, R. Wang, D. T. Liang, and J. H. Tay, Theoretical and experimental studies of membrane wetting in the membrane gas–liquid contacting process for co2 absorption, J. Membr. Sci. **308**, 162 (2008).

[13] J. Wei, W. Jiang, L. Si, X. Xu, and Z. Wen, Experimental study of wetting effect of surfactant based on dynamic wetting process and impedance response of coal, Environ. Sci. Pollut. Res. **30**, 4278 (2023).

[14] V. Lombardi, M. La Rocca, A. Montessori, S. Succi, and P. Prestininzi, On the fate of a drop jumping over a gap, J. Fluid Mech. **949**, A27 (2022).

[15] A. Mukherjee and S. G. Kandlikar, Numerical study of single bubbles with dynamic contact angle during nucleate pool boiling, Int. J. Heat Mass Transf. **50**, 127 (2007).

[16] G. Falcucci, S. Ubertini, D. Chiappini, and S. Succi, Modern lattice Boltzmann methods for multiphase microflows, IMA J. Appl. Math. **76**, 712 (2011).

[17] G. Chaudhary and R. Li, Freezing of water droplets on solid surfaces: An experimental and numerical study, Exp. Therm Fluid Sci. **57**, 86 (2014).

[18] A. Montessori, A. Tiribocchi, M. Lauricella, F. Bonaccorso, and S. Succi, Wet to dry self-transitions in dense emulsions: From order to disorder and back, Phys. Rev. Fluids **6**, 023606 (2021).

[19] G. Falcucci, G. Amati, P. Fanelli, V. K. Krastev, G. Polverino, M. Porfiri, and S. Succi, Extreme flow simulations reveal skeletal adaptations of deep-sea sponges, Nature (London) **595**, 537 (2021).

[20] Z. Guo and C. Shu, *Lattice Boltzmann Method and its Application in Engineering*, Vol. 3 (World Scientific, Singapore, 2013).

[21] G. Falcucci, S. Ubertini, C. Biscarini, S. Di Francesco, D. Chiappini, S. Palpacelli, A. De Maio, and S. Succi, Lattice Boltzmann methods for multiphase flow simulations across scales, Commun. Comput. Phys. **9**, 269 (2011).

[22] A. Montessori and G. Falcucci, *Lattice Boltzmann Modeling of Complex Flows for Engineering Applications* (Morgan & Claypool, San Rafael, CA, 2018).

[23] H. Liu, L. Wu, Y. Ba, G. Xi, and Y. Zhang, A lattice Boltzmann method for axisymmetric multicomponent flows with high viscosity ratio, J. Comput. Phys. **327**, 873 (2016).

[24] Y. Ba, H. Liu, Q. Li, Q. Kang, and J. Sun, Multiple-relaxation-time color-gradient lattice Boltzmann model for simulating two-phase flows with high density ratio, Phys. Rev. E **94**, 023310 (2016).

[25] T. Akai, B. Bijeljic, and M. J. Blunt, Wetting boundary condition for the color-gradient lattice Boltzmann method: Validation with analytical and experimental data, Adv. Water Resour. **116**, 56 (2018).

[26] L. Chen, Q. Kang, Y. Mu, Y.-L. He, and W.-Q. Tao, A critical review of the pseudopotential multiphase lattice Boltzmann model: Methods and applications, Int. J. Heat Mass Transf. **76**, 210 (2014).

[27] Q. Li, K. Luo, and X. Li, Lattice Boltzmann modeling of multiphase flows at large density ratio with an improved pseudopotential model, Phys. Rev. E **87**, 053301 (2013).

[28] G. Falcucci, S. Ubertini, and S. Succi, Lattice Boltzmann simulations of phase-separating flows at large density ratios: the case of doubly-attractive pseudo-potentials, Soft Matter **6**, 4357 (2010).

[29] Q. Li and A. Wagner, Symmetric free-energy-based multicomponent lattice Boltzmann method, Phys. Rev. E **76**, 036701 (2007).

[30] M. Soomro, L. F. Ayala, C. Peng, and O. M. Ayala, Fugacity-based lattice Boltzmann method for multicomponent multiphase systems, Phys. Rev. E **107**, 015304 (2023).

[31] Z. Guo, Well-balanced lattice Boltzmann model for two-phase systems, Phys. Fluids **33**, 031709 (2021).

[32] A. Fakhari and M. H. Rahimian, Phase-field modeling by the method of lattice Boltzmann equations, Phys. Rev. E **81**, 036707 (2010).

[33] S. Shu and N. Yang, Direct numerical simulation of bubble dynamics using phase-field model and lattice Boltzmann method, Ind. Eng. Chem. Res. **52**, 11391 (2013).

[34] L. Yue, Z. Chai, H. Wang, and B. Shi, Improved phase-field-based lattice Boltzmann method for thermocapillary flow, Phys. Rev. E **105**, 015314 (2022).

[35] S. Zhang, J. Tang, and H. Wu, Simplified wetting boundary scheme in phase-field lattice Boltzmann model for wetting phenomena on curved boundaries, Phys. Rev. E **108**, 025303 (2023).

[36] N. S. Martys and H. Chen, Simulation of multicomponent fluids in complex three-dimensional geometries by the lattice Boltzmann method, Phys. Rev. E **53**, 743 (1996).

[37] D. Iwahara, H. Shinto, M. Miyahara, and K. Higashitani, Liquid drops on homogeneous and chemically heterogeneous surfaces: A two-dimensional lattice Boltzmann study, Langmuir **19**, 9086 (2003).

[38] H. Ding and P. D. Spelt, Wetting condition in diffuse interface simulations of contact line motion, Phys. Rev. E **75**, 046708 (2007).

[39] L. Wang, H. B. Huang, and X. Y. Lu, Scheme for contact angle and its hysteresis in a multiphase lattice Boltzmann method, Phys. Rev. E **87**, 013301 (2013).

[40] H. R. Liu and H. Ding, A diffuse-interface immersed-boundary method for two-dimensional simulation of flows with moving contact lines on curved substrates, J. Comput. Phys. **294**, 484 (2015).

[41] J. Huang, J. Wu, and H. Huang, An alternative method to implement contact angle boundary condition and its application in hybrid lattice-Boltzmann finite-difference simulations of two-phase flows with immersed surfaces, Eur. Phys. J. E **41**, 17 (2018).

[42] J. Huang and L. Zhang, Simplified method for wetting on curved boundaries in conservative phase-field lattice-Boltzmann simulation of two-phase flows with large density ratios, Phys. Fluids **34**, 082101 (2022).

[43] A. Briant, Lattice Boltzmann simulations of contact line motion in a liquid-gas system, Philos. Trans. R. Soc. London, Ser. A **360**, 485 (2002).

[44] A. Briant and J. Yeomans, Lattice Boltzmann simulations of contact line motion. ii. binary fluids, Phys. Rev. E **69**, 031603 (2004).

[45] T. Lee and L. Liu, Wall boundary conditions in the lattice Boltzmann equation method for nonideal gases, Phys. Rev. E **78**, 017702 (2008).

[46] L. Liu and T. Lee, Wall free energy based polynomial boundary conditions for non-ideal gas lattice Boltzmann equation, Int. J. Mod. Phys. C **20**, 1749 (2009).

[47] T. Qian, X.-P. Wang, and P. Sheng, Molecular scale contact line hydrodynamics of immiscible flows, Phys. Rev. E **68**, 016306 (2003).

[48] W. Villanueva and G. Amberg, Some generic capillary-driven flows, Int. J. Multiphase Flow **32**, 1072 (2006).

[49] V. Khatavkar, P. Anderson, and H. Meijer, Capillary spreading of a droplet in the partially wetting regime using a diffuse-interface model, J. Fluid Mech. **572**, 367 (2007).

[50] K. Connington and T. Lee, Lattice Boltzmann simulations of forced wetting transitions of drops on superhydrophobic surfaces, J. Comput. Phys. **250**, 601 (2013).

[51] K. W. Connington, T. Lee, and J. F. Morris, Interaction of fluid interfaces with immersed solid particles using the lattice Boltzmann method for liquid–gas–particle systems, J. Comput. Phys. **283**, 453 (2015).

[52] A. Fakhari and D. Bolster, Diffuse interface modeling of three-phase contact line dynamics on curved boundaries: A lattice Boltzmann model for large density and viscosity ratios, J. Comput. Phys. **334**, 620 (2017).

[53] A. Fakhari, Y. Li, D. Bolster, and K. T. Christensen, A phase-field lattice Boltzmann model for simulating multiphase flows in porous media: Application and comparison to experiments of co2 sequestration at pore scale, Adv. Water Resour. **114**, 119 (2018).

[54] C. Zhang, Z. Guo, and Y. Li, A fractional step lattice Boltzmann model for two-phase flow with large density differences, Int. J. Heat Mass Transf. **138**, 1128 (2019).

[55] H. Liang, J. Xu, J. Chen, H. Wang, Z. Chai, and B. Shi, Phase-field-based lattice Boltzmann modeling of large-density-ratio two-phase flows, Phys. Rev. E **97**, 033309 (2018).

[56] Z. Guo, C. Zheng, and B. Shi, Discrete lattice effects on the forcing term in the lattice Boltzmann method, Phys. Rev. E **65**, 046308 (2002).

[57] L. Ju, P. Liu, B. Yan, J. Bao, S. Sun, and Z. Guo, A well-balanced lattice Boltzmann model for binary fluids based

on the incompressible phase-field theory, arXiv:2311.10827 [Commun. Comput.Phys. (to be published)].

[58] H. Liang, B. Shi, Z. Guo, and Z. Chai, Phase-field-based multiple-relaxation-time lattice Boltzmann model for incompressible multiphase flows, Phys. Rev. E **89**, 053320 (2014).

[59] M. R. Moldover and J. W. Cahn, An interface phase transition: complete to partial wetting, Science **207**, 1073 (1980).

[60] H. Liang, H. Liu, Z. Chai, and B. Shi, Lattice Boltzmann method for contact-line motion of binary fluids with high density ratio, Phys. Rev. E **99**, 063306 (2019).

[61] Y. Yan and Y. Zu, A lattice Boltzmann method for incompressible two-phase flows on partial wetting surface with large density ratio, J. Comput. Phys. **227**, 763 (2007).

[62] T. Young, III. An essay on the cohesion of fluids, Philos. Trans. R. Soc. London **95**, 65 (1805).

[63] X. Li, J. Lowengrub, A. Rätz, and A. Voigt, Solving pdes in complex geometries: a diffuse domain approach, Commun. Math. Sci. **7**, 81 (2009).

[64] Q. Li, Y. Yu, and K. H. Luo, Implementation of contact angles in pseudopotential lattice Boltzmann simulations with curved boundaries, Phys. Rev. E **100**, 053313 (2019).

[65] S. Whitaker, *The Method of Volume Averaging*, Vol. 13 (Springer Science & Business Media, New York, 1998).

[66] C. Soulaine, S. Roman, A. Kovscek, and H. A. Tchelepi, Mineral dissolution and wormholing from a pore-scale perspective, J. Fluid Mech. **827**, 457 (2017).

[67] X. Liu, Z. Chai, C. Zhan, B. Shi, and W. Zhang, A diffuse-domain phase-field lattice Boltzmann method for two-phase flows in complex geometries, Multiscale Model. Simul. **20**, 1411 (2022).

[68] S. Mao, D. Kuldinow, M. P. Haataja, and A. Košmrlj, Phase behavior and morphology of multicomponent liquid mixtures, Soft Matter **15**, 1297 (2019).

[69] G. Negro, L. N. Carenza, G. Gonnella, F. Mackay, A. Morozov, and D. Marenduzzo, Yield-stress transition in suspensions of deformable droplets, Sci. Adv. **9**, eadf8106 (2023).

[70] L. Carenza, G. Gonnella, A. Lamura, D. Marenduzzo, G. Negro, and A. Tiribocchi, Soft channel formation and symmetry breaking in exotic active emulsions, Sci. Rep. **10**, 15936 (2020).

[71] G. Negro, A. Lamura, G. Gonnella, and D. Marenduzzo, Hydrodynamics of contraction-based motility in a compressible active fluid, Europhys. Lett. **127**, 58001 (2019).